Catalysis Communications 178 (2023) 106677

Contents lists available at ScienceDirect

Catalysis Communications

journal homepage: www.elsevier.com/locate/catcom

Sr-doped calcium and barium manganites as catalysts in heterogeneous oxidation of volatile organic compounds

Andreja Žužić [a,*], Filip Car [a], Jelena Macan [a], Vesna Tomašić [a], Andreja Gajović [b]

[a] University of Zagreb Faculty of Chemical Engineering and Technology, Marulićev trg 19, HR-10000 Zagreb, Croatia
[b] Ruđer Bošković Institute, Bijenička cesta 54, HR-10000 Zagreb, Croatia

ARTICLE INFO

Keywords:
Autocombustion synthesis
Barium manganites
Calcium manganites
Catalytic oxidation
Coprecipitation
Volatile organic compounds

ABSTRACT

Sr-doped $CaMnO_3$ and $BaMnO_3$ were prepared by autocombustion (CNA) and coprecipitation and investigated as catalysts for catalytic oxidation of benzene, toluene, ethylbenzene and *o*-xylene mixture in a fixed-bed reactor. Ethylbenzene and *o*-xylene were completely removed by all prepared catalysts. Toluene was completely removed by $BaMnO_3$ and $Ba_{0.5}Sr_{0.5}MnO_3$ catalysts prepared by CNA synthesis, while conversions of ~98% or higher were obtained for all the other prepared catalysts. The highest benzene conversion of 86.43% at 723 K was obtained for the $Ba_{0.7}Sr_{0.3}MnO_3$ catalyst prepared by CNA synthesis. The differences in catalytic activities can be ascribed to Sr-doping, oxygen nonstoichiometry and morphological differences.

1. Introduction

Volatile organic compounds (VOCs) are organic solvents that evaporate easily under normal conditions (atmospheric pressure and room temperature) [1]. High VOC emissions can lead to the formation of ground-level ozone [2], and VOC exposure can cause harmful health effects, such as allergic sensitization, respiratory diseases, lung function damage and gene mutation [3,4].

To decrease outdoor VOC emissions, the VOCs released from the industrial processes must be recovered (by absorption, adsorption, condensation and membrane separation) or destroyed [5,6]. Destruction methods are commonly applied to remove VOCs from the air. The bacterial conversion of organic pollutants into water, carbon dioxide and biomass under aerobic conditions is both efficient and inexpensive, yet it cannot remove compounds with high molecular weights, low solubility and complex structures (e.g. chlorinated hydrocarbons) [5]. Thermal oxidation or combustion of VOCs is usually performed at temperatures between 973 and 1273 K, although the process will require higher temperatures or longer times in the combustion zone for more resistant compounds. The high temperatures can result in the formation of nitrogen oxides as secondary pollutants, while halogenated compounds are often converted to hydrohalogenic acids which can cause the corrosion of equipment [5,7].

Catalytic oxidation is thus often a better alternative to thermal oxidation, as the appropriate catalyst lowers the operating temperature to the 373–723 K range and enables complete oxidation of VOCs into CO_2 and H_2O. Catalytic oxidation can be applied for diluted effluent streams containing <1% of VOCs and made more energy-efficient by coupling it with a heat exchanger [8]. Highly stable noble metals, especially Pd, are preferred catalysts in the industrial removal of VOCs [9], and metal oxides, such as perovskites, present a promising alternative for the catalytic oxidation of VOCs. Perovskites can be described with an ABO_3 formula: the A-site is occupied by an alkaline-earth or rare-earth metal ion, while the B-site is occupied by the transition metal ion octahedrally coordinated by oxygen anions. Since transition metal ions (B) can have a variety of valences, perovskites often exhibit cation or oxygen nonstoichiometry [10].

The research was focused on the rare-earth perovskites (A = La, Sm) and the effect of different B-site cations on the catalytic activity. $LaMnO_3$ was found to possess higher catalytic activity (lower activation energy) than $LaFeO_3$ for the oxidation of toluene due to the higher reducibility of Mn [11]. Investigation of toluene oxidation over $SmMnO_3$ perovskite catalyst [12] obtained similar results, with toluene being completely oxidized at 573 K. These two independent studies on different manganites have shown the importance of the role of B-site cation in catalytic activity. However, the influence of different combinations of A-site alkaline-earth cations on the catalytic activity of perovskites is less investigated. The authors' previous research [13,14] has shown that different synthesis methods and Sr-substitution levels affect the crystal structure and oxygen nonstoichiometry of $CaMnO_3$ and $BaMnO_3$.

* Corresponding author.
E-mail address: azuzic@fkit.unizg.hr (A. Žužić).

https://doi.org/10.1016/j.catcom.2023.106677
Received 21 February 2023; Received in revised form 20 April 2023; Accepted 21 April 2023
Available online 25 April 2023

Therefore, this study aims to investigate how different alkaline-earth A-site cations, their substitution level and synthesis methods impact the catalytic activity of manganites for the simultaneous oxidation of four volatile organic compounds; benzene, toluene, ethylbenzene and *o*-xylene, abbreviated to BTEX.

2. Materials and methods

2.1. Preparation of $Ca_{1-x}Sr_xMnO_3$ and $Ba_{1-x}Sr_xMnO_3$ catalysts

$Ca_{1-x}Sr_xMnO_3$ (CSMO) and $Ba_{1-x}Sr_xMnO_3$ (BSMO) catalysts ($x = 0$, 0.3 and 0.5) were synthesized using citrate-nitrate autocombustion (CNA) and coprecipitation, as detailed in [13]. Briefly, $CaCO_3$ (99.8%, VWR Chemicals), $SrCO_3$ (99.5%, Alfa Aesar GmbH), $BaCO_3$ (99%, Kemika) and $Mn(NO_3)_2 \bullet 4H_2O$ (97.5%, Fisher Scientific) were dissolved in 0.5 M HNO_3 (Riedel-de Haën), and then complexed by the addition of citric acid ($C_6H_8O_7$, min. 99.5%, Gram-mol d.o.o.) in excess (molar ratio of citric acid and metal ions was 3). The prepared solution was heated to 773 K, and a dark yellow gel was formed. The continued heating resulted in the autocombustion of the reaction mixture and the formation of a dark brown precursor powder which was ground in an agate mortar and calcined at 1473 K/2 h. The CSMO samples were designated as CL_Sr0, CL_Sr0.3 and CL_Sr0.5, while the BSMO samples were designated as BL_Sr0, BL_Sr0.3 and BL_Sr0.5.

In coprecipitation synthesis, the solution of metal cations was added dropwise into the 10 wt% solution of NH_4HCO_3 (min. 99%, Honeywell) in 50% excess, heated at 338 K. To ensure complete coprecipitation of all present metal cations, the pH value of the reaction mixture was maintained at 8 by the addition of aqueous ammonia (NH_3, 28%, VWR Chemicals). The obtained precipitates were filtrated, washed with filtrate and several times with distilled water, dried for one day at room temperature and calcined at 1473 K/2 h. The obtained CSMO samples were designated as CC_Sr0, CC_Sr0.3 and CC_Sr0.5. The prepared BSMO samples were designated as BC_Sr0, BC_Sr0.3 and BC_Sr0.5.

2.2. Characterization of the prepared catalysts

The content of oxygen vacancies and Mn average oxidation states in prepared CSMO and BSMO catalysts were determined by permanganate titration as described in [14].

Phase analysis of CSMO and BSMO catalysts was performed by X-ray powder diffraction measurements (XRD) followed by the Rietveld refinement analysis. Diffractograms were obtained using Shimadzu XRD-6000 diffractometer with CuKα (1.5406 Å) radiation, operating at 40 kV and 30 mA, with a 2Θ range of 20–70° at a step size of 0.02° and exposure of 4.5 s. The Rietveld refined profiles were obtained in the FullProf Suite software as detailed in [13].

The Raman spectroscopy (RS) measurements were performed using Horiba, JobineYvon T64000 spectrometer with the solid-state laser operating at 532 nm for the excitation. The Raman spectra were collected in micro-Raman mode with a multi-channel CCD detector. A laser power of 20 mW at the sample and an objective with a 50 magnification with a long working distance were used. With the aim to improve the signal-to-noise ratio, spectra were recorded using multi-scan mode; 10 scans for every segment of the spectrum with 60 s accumulation of each scan.

The morphology of CSMO and BSMO catalysts was investigated by scanning electron microscopy (SEM) on Tescan Vega 3 Easyprobe microscope operating at 10 kV. The information about the atom occupancies was obtained by energy dispersive spectroscopy (EDS) using EDS Bruker XFlash 4010-M.

The specific surface areas and average pore diameters of CSMO and BSMO catalysts were determined by N_2 adsorption/desorption analysis at 77 K (instrument Micrometrics ASAP 2000) and calculated using the Brunauer-Emmett-Teller (BET) model. Prior to the analysis, the samples were degassed at 6.6 Pa and 373 K. The pore size distributions were estimated from the N_2 isotherm data using Barret-Joyner-Halenda (BJH) model.

2.3. Catalytic activity testing

Catalytic activity of CSMO and BSMO was tested using an experimental setup shown in the Supplemental Material Fig. S1. As a model mixture of aromatic compounds, a gaseous mixture of benzene, toluene, ethylbenzene, *o*-xylene (BTEX) and nitrogen (50 ppm of each component in nitrogen) was used. The BTEX reaction mixture flow rate was set to 80 $cm^3\ min^{-1}$ and regulated by Brooks mass flow controllers (MFC). 0.05 g of catalyst powder fraction of 70–100 μm in size was immobilized in a fixed bed reactor between quartz wool plugs. The reactor was placed into the heating block with a thermocouple connected to a TC208 Series thermo-controller, and the tests were performed in the 373–723 K temperature range. Every data point is an average of three consecutive steady-state measurements at each temperature. The initial and final concentrations of the BTEX mixture were analyzed by on-line gas chromatography using a Shimadzu GC-2014 with a flame ionization detector (FID). The conversion (X_A) of each organic compound was calculated as the ratio of the final and the initial concentration.

3. Results and discussion

3.1. CSMO and BSMO crystallization

Crystallization of desired CSMO and BSMO catalysts was confirmed by XRD and EDS analysis, as shown graphically and numerically in the Supplemental Material Figs. S2 and S3, and Tables S1 and S2. Oxygen content determined from atom occupancies (δ_{calc}) matched the results of permanganate titration (δ_{exp}), both shown in Table 1.

All CSMO catalysts have crystallized in a *Pnma* orthorhombic system. Sr-doping of BSMO caused structural changes: undoped $BaMnO_3$ has crystallized in the rhombohedral system with $R\bar{3}m$ space group, $Ba_{0.7}Sr_{0.3}MnO_3$ has crystallized in hexagonal structure with the same space group, while $Ba_{0.5}Sr_{0.5}MnO_3$ has crystallized in the hexagonal system with *P*63/*mmc* space group. Structural changes of doped $BaMnO_3$ were also reported for $BaMn_{1-x}Ti_xO_3$ ($0 \leq x \leq 0.25$) materials [15].

The Raman spectra of all prepared materials were recorded in the 50–800 cm^{-1} range. Since CSMO spectra showed only a broad fluorescence band, only the spectra of BSMO materials are shown in Fig. 1.

Nine phonon modes (P1 – P9) were observed at room temperature, which matched well with previously reported results for $Ba_{0.9}Sr_{0.1}MnO_3$ [16]. The P1 mode observed at 100 cm^{-1} in all samples and the P2 mode

Table 1
The calculated (δ_{calc}) and experimentally determined (δ_{exp}) oxygen non-stoichiometry and average Mn oxidation state (AOS), the average crystallite size (D) calculated by the Scherrer equation, specific surface area (S_A) and the average pore size diameter (d_p) obtained from N_2 adsorption/desorption analysis.

Sample	δ_{calc}	δ_{exp}	AOS(Mn)	D, nm	S_A, $m^2\ g^{-1}$	d_p, nm
CL_Sr0	−0.032	−0.030	3.936	100	0.45	1.97
CL_Sr0.3	0.008	0	4	92	0.83	2.52
CL_Sr0.5	−0.026	−0.030	3.948	74	0.89	1.19
CC_Sr0	−0.132	−0.130	3.736	89	0.50	4.53
CC_Sr0.3	−0.099	−0.100	3.802	66	0.59	7.54
CC_Sr0.5	−0.071	−0.070	3.858	53	0.72	5.27
BL_Sr0	−0.716	−0.690	2.568	177*	0.70	4.45
BL_Sr0.3	−0.532	−0.532	2.936	57	1.03	5.91
BL_Sr0.5	−0.292	−0.292	3.416	55	1.12	6.04
BC_Sr0	−0.715	−0.710	2.570	166*	0.61	5.67
BC_Sr0.3	−0.621	−0.620	2.758	64	0.78	5.61
BC_Sr0.5	−0.208	−0.210	3.784	54	0.83	6.15

* The Scherrer equation can be applied to determine crystallite size from 100 to 200 nm, but it is not recommended and depends on the instrument characteristics.

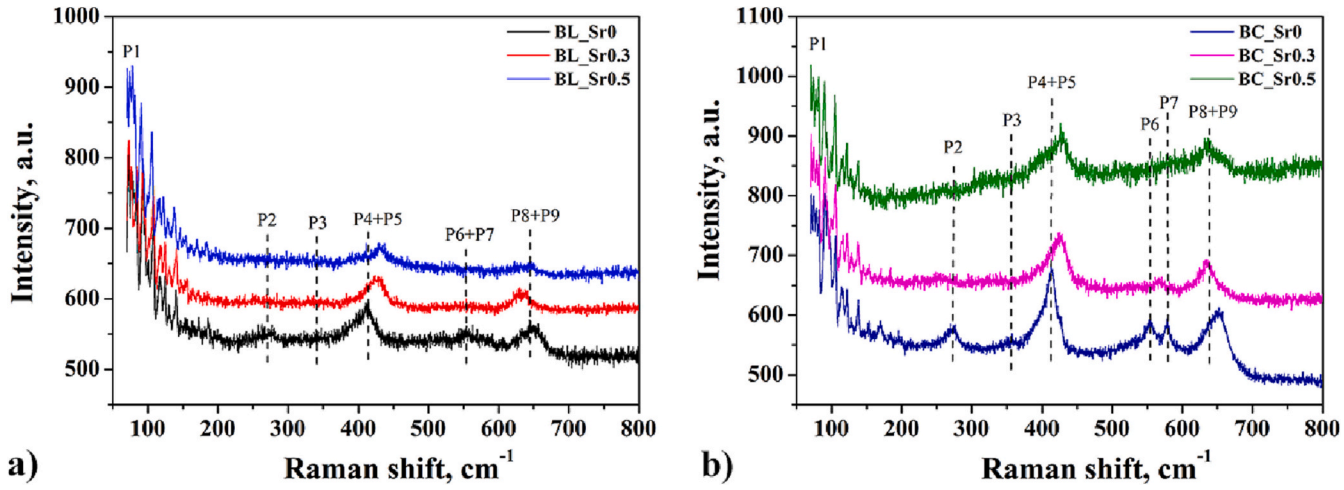

Fig. 1. Raman spectra of BSMO materials prepared by CNA (a) and coprecipitation (b) synthesis with assigned Raman active phonons (P1 – P9).

located at 270 cm^{-1} both originated from Ba vibrations. According to Poojitha et al. [16], both Ba and Sr atoms are included in P2 vibrations. However, in this study, the P2 phonon had the highest intensity in the undoped BL_Sr0 and BC_Sr0 samples, which confirmed that it originated predominantly from Ba vibrations. The third phonon P3 at 344 cm^{-1} originating from Mn vibrations and characteristic of rhombohedral $R\bar{3}m$ crystal structure [15] was observed only in the undoped BL_Sr0 and BC_Sr0 samples. At about 420 cm^{-1}, a wide band originating from overlapping P4 and P5 phonon modes was observed. The P4 mode originated from the Mn vibration, while the P5 mode originated from the O vibrations. The modes P6 – P9 in the 550–650 cm^{-1} range also originated from the O vibrations. The P8 + P9 modes at about 650 cm^{-1} were the broadest in the undoped BL_Sr0 and BC_Sr0 samples, which had the highest oxygen deficiencies (δ_{exp} in Table 1). This is in accordance with the previous studies [17–19], which found that broadened P8 and P9 phonon peaks indicate significant structure distortion related to oxygen deficiency.

3.2. Morphology of prepared catalysts

SEM micrographs of CSMO catalysts (Fig. 2) have revealed expected morphological differences [20]. CNA synthesis has yielded powders with a 'sponge-like' morphology composed of crystalline grains of about 200 nm in diameter due to the extensive gas evolvement in the combustion step of the synthesis procedure [14,21]. On the other hand, CSMO powders obtained by coprecipitation were composed of aggregates. In the CC_Sr0 sample, the largest crystalline grains of about 5 μm in diameter were observed, while the increasing Sr-content resulted in smaller crystalline grains of about 200 nm in diameter, similar to those obtained in the CNA synthesis.

SEM micrographs of BSMO catalysts (Fig. 3) have shown similar 'sponge-like' morphology for both synthesis methods with no significant differences despite increasing Sr-doping and the changes in the crystalline structure. The 'sponge-like' morphology of BSMO powders prepared by coprecipitation synthesis is probably a consequence of extensive CO_2 evolvement during the degradation of carbonate precursors in the calcination step of the synthesis.

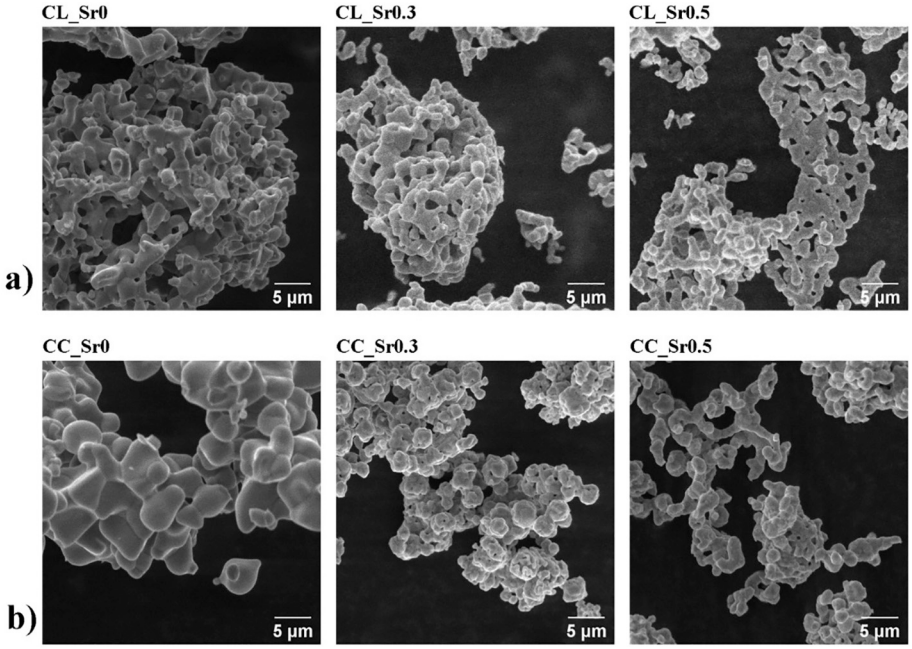

Fig. 2. SEM micrographs of CSMO catalysts prepared by CNA (a) and coprecipitation (b) synthesis.

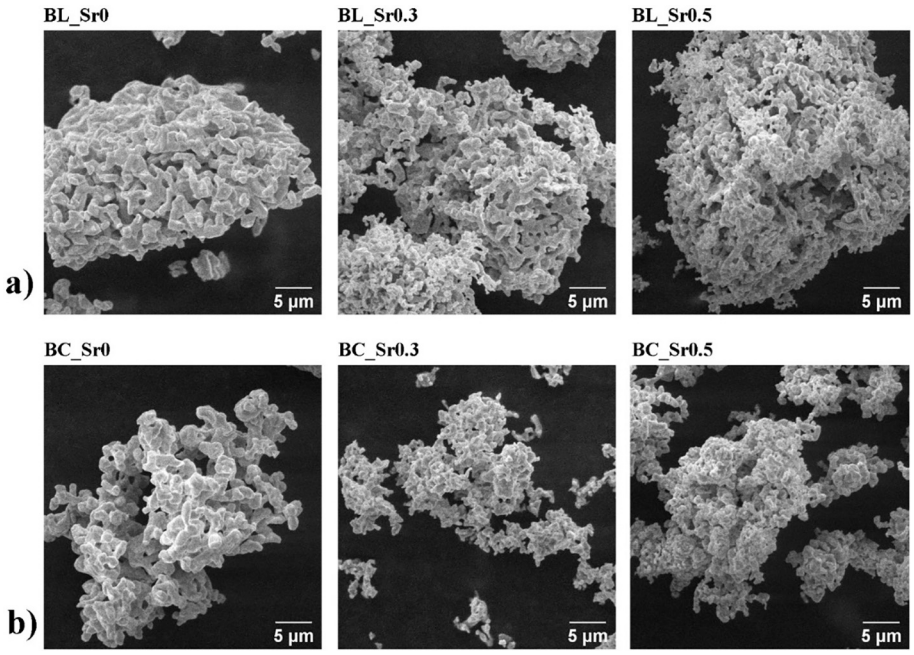

Fig. 3. SEM micrographs of BSMO catalysts prepared by CNA (a) and coprecipitation (b) synthesis.

The average crystallite size (D, nm) was calculated using the Scherrer equation [22]. The specific surface area (S_A, $m^2\ g^{-1}$) and average pore diameter (d_p, nm) were calculated using the BET model as described in Chapter 2.2. The results are shown in Table 1.

CSMO catalysts prepared by coprecipitation had smaller average crystallite sizes than those prepared by CNA. This can be explained by the higher oxygen nonstoichiometry in coprecipitated samples leading to the unit cell distortion and resulting in smaller crystallite volume [20]. Average crystallite sizes did not differ significantly with the preparation method for BSMO catalysts, which might be due to the more uniform oxygen nonstoichiometry for the same Sr content. The average crystallite size decreased with increased Sr-doping for both CSMO and BSMO catalysts. This can be explained by the lattice distortion caused by doping: residual compressive stress increases due to the distortion, resulting in a decrease in the average crystallite size, regardless of the dopant size [23].

The increased Sr-doping also caused an increase in specific surface areas, which remain small (0.83 $m^2\ g^{-1}$–1.12 $m^2\ g^{-1}$) even for the highest doping content of 0.5 (Table 1). The CSMO catalysts prepared by the CNA synthesis possessed a larger specific surface area due to the loose 'sponge-like' morphology. The primary cause of small specific surface areas is the high temperature required to form the target manganite phases. Berbenni et al. [24] and Gagrani et al. [25] obtained high specific surface areas of 39.64 $m^2\ g^{-1}$ and 13.8 $m^2\ g^{-1}$ via solid-state synthesis. However, these non-calcined catalysts may undergo structural changes during exposure to higher temperatures required for the catalytic oxidation of VOCs. On the other hand, Rezlescu et al. [26] have shown that specific surface area is not the main factor contributing to the catalytic activity of perovskites, since the oxygen non-stoichiometry and Mn mixed valences play a significant part.

There was no clear trend between Sr-doping and the average pore diameter since the pore diameter depends on the interparticle porosity and the intragranular pores formed during the sintering. For the CSMO catalysts, significantly larger average pore diameters (4.53–7.54 nm, Table 1) were obtained by coprecipitation synthesis, since the pores between the aggregates (Fig. 2b) were predominant. On the other hand, the average pore diameters of BSMO catalysts did not differ depending on the synthesis procedure for the same Sr-doping content and were in a 4.45–6.15 nm range.

The pore size distributions, estimated using the BJH model, are shown in Fig. 4. The pore size distribution of the CSMO catalysts prepared by CNA synthesis could not be determined due to the low volume of adsorbed N_2. For the other catalysts, a relatively wide interparticle pore size distribution (2–40 nm) preferably placed at lower d_p was observed, similar to the previously investigated LSMO catalysts [20].

3.3. CSMO and BSMO catalytic activity

Conversion curves for BTEX oxidation (Figs. 5 and 6) were S-shaped and characteristic of the first-order chemical reactions [20,27]. Temperatures corresponding to 10% (T_{10}), 50% (T_{50}) and 90% (T_{90}) conversions are given in the Supplemental Material Tables S3 and S4. The final BTEX conversions (X_A) of each component are shown in Table 2 for all prepared catalysts.

At the final temperature of 723 K, ethylbenzene and *o*-xylene were completely removed using all prepared catalysts, since these compounds possess larger substituents which are more easily susceptible to removal by bond scission. Toluene was completely removed using CL_Sr0.3, CL_Sr0.5, CC_Sr0.3, CC_Sr0.5, BL_Sr0.3 and BL_Sr0.5. Slightly lower but satisfying results above 97% were obtained for undoped CSMO and BSMO catalysts, as well as for Sr-doped BSMO catalysts prepared by coprecipitation. The lowest conversions, below 70%, were observed for CL_Sr0.5 and CC_Sr0. Among all model compounds, benzene is the most stable and requires the highest temperatures for complete conversion, which could not be achieved using the present experimental setup. The maximum achieved conversion of benzene at 723 K was 86.43% obtained by using BL_Sr0.3 as a catalyst. This was 6% higher in comparison to the $La_{0.7}Sr_{0.3}MnO_3$ (LL_Sr0.3) [20], which makes BSMO a low-cost alternative to the LSMO catalysts. No clear trend was found when comparing the influence of Sr-doping, synthesis method and average Mn oxidation state on the benzene conversion at 723 K (Fig. 7).

Higher benzene conversions were obtained for the Sr-doped CSMO catalysts prepared by coprecipitation than those prepared by the CNA method. The CSMO catalysts prepared by coprecipitation had more oxygen vacancies, lower Mn oxidation state, and larger average pore diameters (Table 1), resulting in better oxygen mobility and diffusion of reactants and products. On the other hand, BSMO catalysts prepared by CNA synthesis have shown higher benzene conversions than the

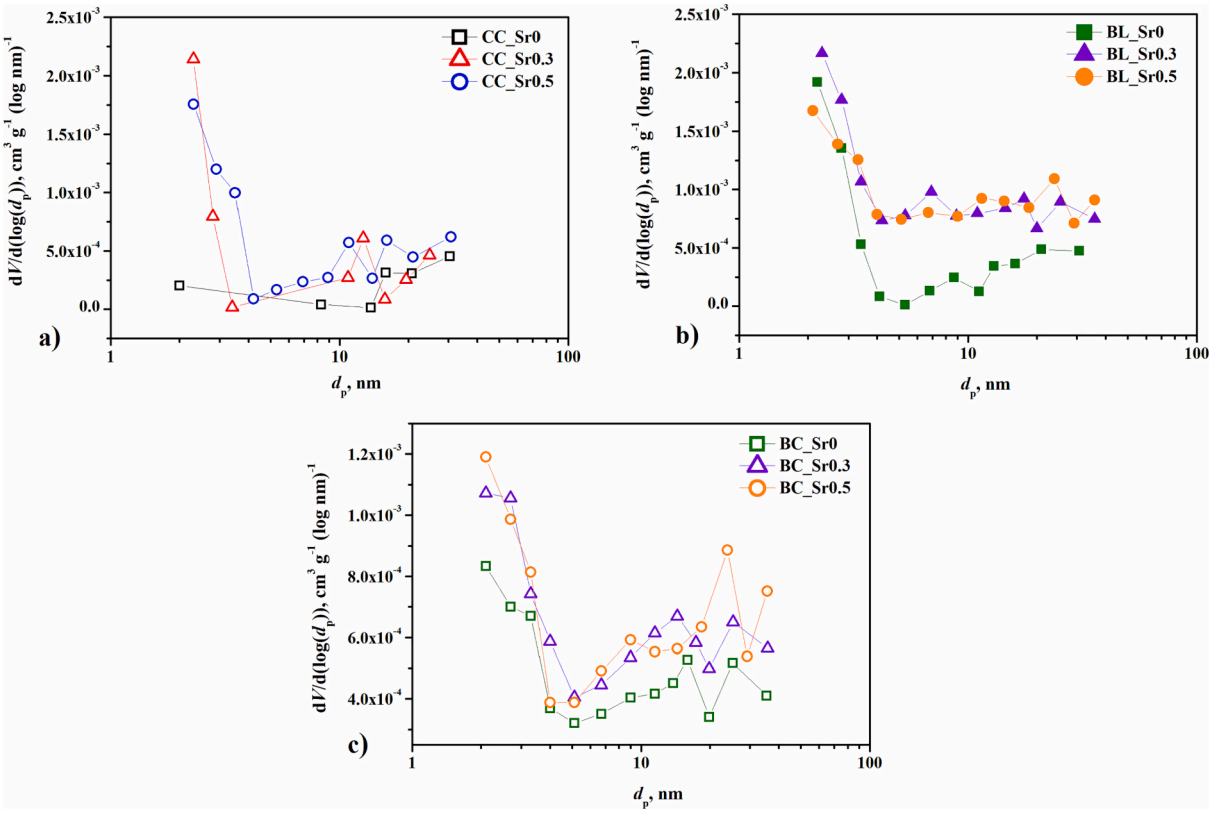

Fig. 4. Pore size distributions of CSMO catalysts prepared by coprecipitation (a) and BSMO catalysts prepared by CNA (b) and coprecipitation (c) synthesis.

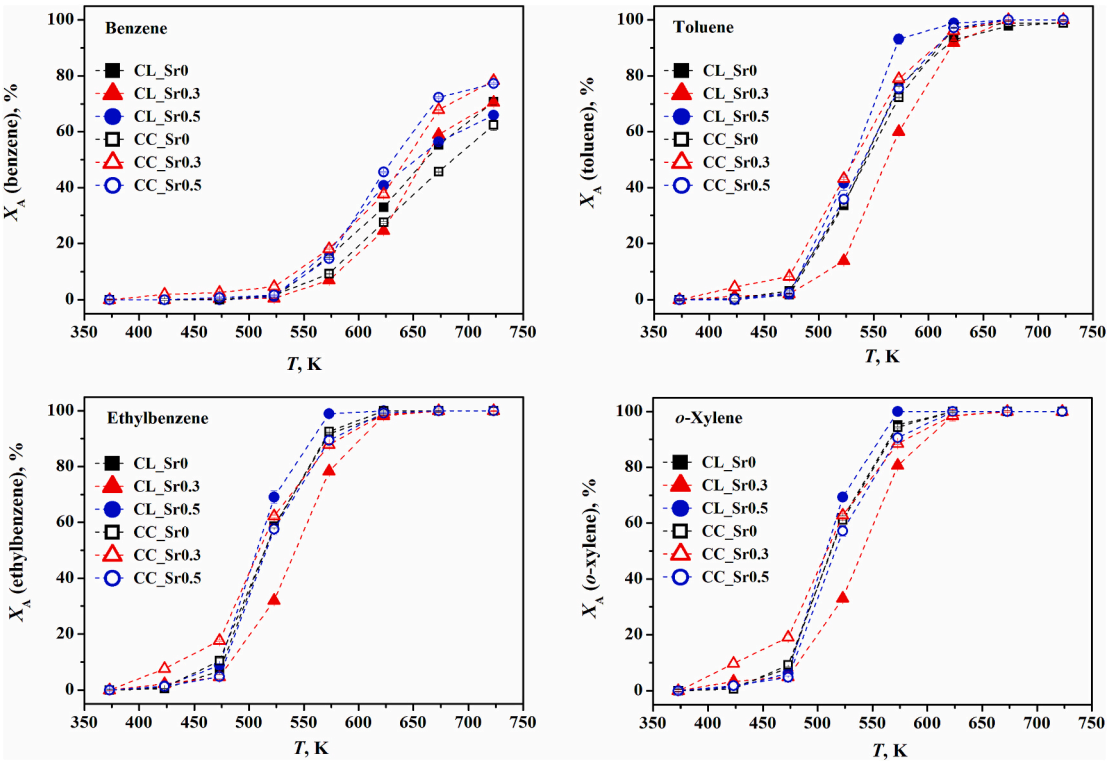

Fig. 5. Conversions of benzene, toluene, ethylbenzene and *o*-xylene as a function of reaction temperature for CSMO catalysts.

coprecipitated catalysts. Since oxygen nonstoichiometry and average pore diameters did not significantly differ for BSMO with the same *x*, the observed differences might be due to the larger specific surface area (Table 1) of catalysts prepared by CNA. The exception was the undoped BC_Sr0 sample, which achieved about 5% higher benzene conversion than BL_Sr0. Moreover, it was observed that the highest benzene

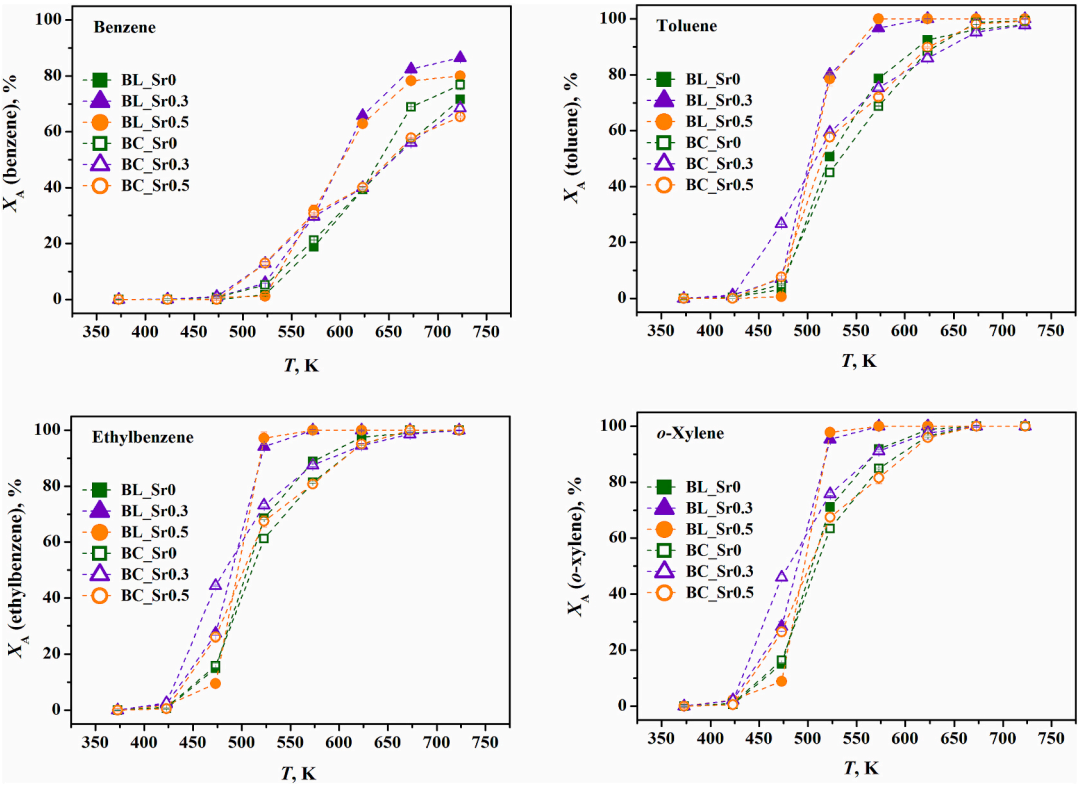

Fig. 6. Conversions of benzene, toluene, ethylbenzene and *o*-xylene as a function of reaction temperature for BSMO catalysts.

Table 2
The final BTEX conversions (X_A) at 723 K for CSMO and BSMO catalysts.

Sample	$X_{A(B,\ 723)}$, %	$X_{A(T,\ 723)}$, %	$X_{A(E,\ 723)}$, %	$X_{A(X,\ 723)}$, %
CL_Sr0	70.77	99.03	100	100
CL_Sr0.3	70.49	100	100	100
CL_Sr0.5	65.96	100	100	100
CC_Sr0	62.33	98.90	100	100
CC_Sr0.3	78.34	100	100	100
CC_Sr0.5	77.25	100	100	100
BL_Sr0	71.69	97.93	100	100
BL_Sr0.3	86.43	100	100	100
BL_Sr0.5	79.98	100	100	100
BC_Sr0	76.89	99.39	100	100
BC_Sr0.3	68.46	97.89	100	100
BC_Sr0.5	65.32	99.28	100	100

conversion at 723 K was achieved using CSMO and BSMO catalysts with an average Mn oxidation state of 3.802 and 2.936, respectively. The significantly lower oxidation state of BSMO catalysts required for the same catalytic activity might be the result of the lower cell distortion in barium manganites, which was estimated using Goldschmidt's tolerance factor, *t* [28]:

$$t = \frac{(r_A + r_O)}{\sqrt{2}(r_B + r_O)}. \quad (1)$$

In this equation, *r* represents the ionic radius of A- and B-site cations and oxygen anion. Even though the equation was derived from the bond lengths in an ideal cubic perovskite cell, it can be extended to different distorted perovskite structures [29]. The tolerance factor for CSMO catalysts was about 0.89, indicating a distorted structure, while BSMO catalysts had a tolerance factor of 1, characteristic of the ideal non-distorted structure. Therefore, it is likely that higher oxygen non-stoichiometry and lower Mn average oxidation state of BSMO catalysts are required to cause cell distortion and promote oxygen mobility through the lattice.

The ratio of Mn^{4+}/Mn^{3+} in the manganite structure, i.e., the Mn average oxidation state, is very important for the catalytic activity since it determines the amount of active oxygen species (O^{2-}, O_2^- and O^-) which react in catalytic oxidation following a Mars-van Krevelen mechanism [30,31]. In the first step of the Mars-van Krevelen mechanism, the molecules adsorbed on the surface of the catalyst (R_{ads}) are oxidized by the oxygen atom from the oxide lattice ($O^{2-}_{lattice}$), resulting in the formation of the oxidation products (—R—O) and oxygen vacancies (—□—) on the surface of the catalyst, while the metal ions change towards a lower valence state ($M^{(n-1)+}$):

$$R_{ads} + \left(—M^{n+}—O^{2-}—M^{n+}—\right) \rightarrow (—R—O) + \left(—M^{(n-1)+}—□—M^{(n-1)+}—\right) \quad (2)$$

The number of active sites is determined by the structural defects generated by the Mn^{4+}/Mn^{3+} ratio in the manganite structure and by the preparation method. Reoxidation of the catalyst surface, as the next step of the catalytic oxidation, can occur either directly by oxidation with the oxygen in the gas phase (which is usually adsorbed on the anion vacancies near reduced metallic ions, $M^{(n-1)+}$):

$$2\left(—M^{(n-1)+}—□—M^{(n-1)+}—\right) + O_2 \rightarrow 2\left(—M^{n+}—O^{2-}—M^{n+}—\right) \quad (3)$$

or indirectly, due to the diffusion of the oxygen atoms from the oxide bulk to the reduced sites on the surface of the catalyst.

To our best knowledge, this paper represents the first study of CSMO and BSMO as catalysts in heterogeneous oxidation catalysis of a gaseous mixture of aromatic compounds. However, the catalytic activity of these materials has been confirmed for other applications. $CaMnO_3$ catalysts with the addition of Na_2WO_4 were efficient for the oxidative naphtha cracking into olefines [32,33] since the ionic and electronic conductivity of the surface Na_2WO_4 layer led to selective O^{2-} transportation. Dewi et al. [34] prepared $CaMnO_3$ catalysts via CNA synthesis and proved their catalytic activity for the degradation of methylene blue dye using hydrogen peroxide as an oxidant. $CaMnO_3$ was able to degrade 98.5% of the dye within 20 min in solution at pH 2. Furthermore, Wang et al. [35]

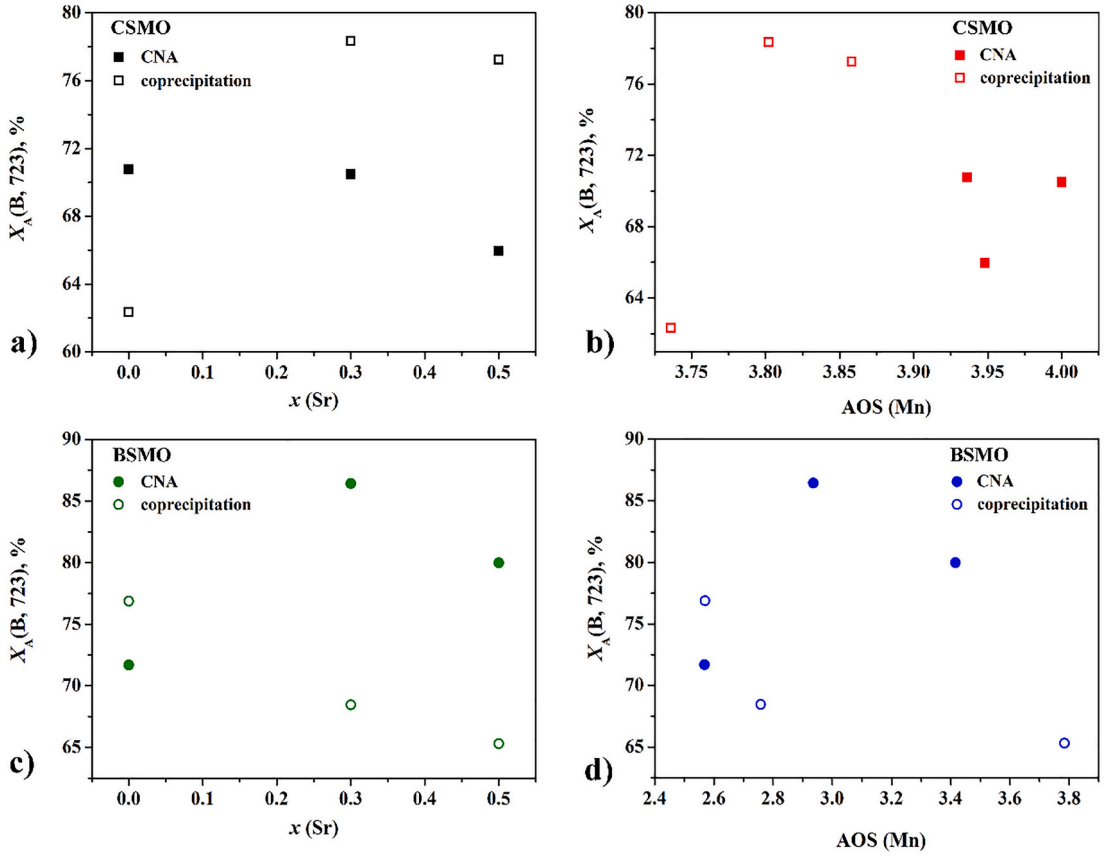

Fig. 7. Conversions of benzene (X_A(B, 723), %) at 723 K as a function of Sr-doping (x) and Mn average oxidation state on CSMO (a, b) and BSMO (c, d) catalysts.

showed that $CaMnO_3$ catalysts possess great potential in organic pollutants' removal by catalytic activation of peroxydisulfate in alkaline solutions. $BaMnO_3$ catalysts have shown higher syngas selectivity and coke resistance than the $CaMnO_3$ catalysts in the conventional methane reforming process [36] due to the higher amount of loosely bounded oxygen ions in $CaMnO_3$ leading to a non-selective behaviour. Ning et al. [37] have prepared $BaMnO_3$-CeO_2 composite catalyst for direct nitrogen monoxide (NO) decomposition into N_2 and O_2. The achieved NO conversion to N_2 was 57.1% for the catalyst thermally treated at 800 °C due to the high amount of oxygen vacancies promoting oxygen adsorption and mobility. Ye et al. [38] supported conventional Cu-based catalyst with $BaMnO_3$, which resulted in the formation of $BaMnO_3$ nanocrystals in mesoporous Cu-based catalyst and improved the oxidation process of NO to NO_2. Additionally, $CaMnO_3$ and $BaMnO_3$ catalysts have a great potential for application in solid oxide electrolysis cells for H_2 and O_2 production by water splitting [31,39]. Therefore, CSMO and BSMO are promising catalysts for multiple applications because of their catalytic activity and stability in aqueous solutions and gas phases. Their catalytic activity can be modified by doping, controlling morphology and adding the surface layers for selective oxygen transportation. Further improvements could be achieved by annealing under the reducing atmosphere to enhance oxygen vacancies and by adding pore-forming agents to control the porosity of catalysts [40,41].

4. Conclusion

CSMO and BSMO catalysts were successfully synthesized by CNA and coprecipitation procedure and investigated for heterogeneous oxidation catalysis of the BTEX mixture. The catalysts were predominantly mesoporous, with specific surface areas ranging from 0.45 to 1.12 $m^2\ g^{-1}$. Complete degradation of ethylbenzene and *o*-xylene was achieved using all prepared catalysts. Toluene was fully degraded with all Sr-doped CSMO catalysts, BL_Sr0.3 and BL_Sr0.5, while the other catalysts resulted in conversions of about 97%. The 100% conversion of benzene was not achieved due to its high stability. The maximum conversion of 86.43% was achieved using the BL_Sr0.3 catalyst, which is 6% higher than the previously investigated LSMO catalyst. In summary, coprecipitation synthesis yielded more active CSMO catalysts due to their lower average Mn oxidation state and larger average pore volume. On the other hand, the CNA procedure was more suitable for the BSMO catalysts since it yielded materials with larger specific surface areas. Therefore, CSMO and BSMO were shown to be promising low-cost catalysts in the catalytic oxidation of aromatic compounds.

CRediT authorship contribution statement

Andreja Žužić: Conceptualization, Investigation, Visualization, Writing – original draft. **Filip Car:** Formal analysis, Investigation, Visualization. **Jelena Macan:** Supervision, Writing – review & editing. **Vesna Tomašić:** Project administration, Supervision, Writing – review & editing. **Andreja Gajović:** Investigation, Visualization, Project administration, Writing – review & editing.

Declaration of Competing Interest

The authors declare that they have no known competing financial interests or personal relationships that could have appeared to influence the work reported in this paper.

Data availability

Data will be made available on request.

Acknowledgements

This work has been supported in part by Croatian Science Foundation under the projects IP-2018-01-5246, IP-2018-01-8669, and by the Virtulab Project (KK.01.1.1.02.0022) co-funded by the European Regional Development Fund.

Appendix A. Supplementary data

Supplementary data to this article can be found online at https://doi.org/10.1016/j.catcom.2023.106677.

References

[1] S.S. Anand, B.K. Philip, H.M. Mehendale, Volatile organic compounds, in: P. Wexler (Ed.), Encyclopedia of Toxicology, 3rd ed, Elsevier, 2014, pp. 967–970, https://doi.org/10.1016/B978-0-12-386454-3.00358-4.
[2] J.F. Lamonier, Catalytic removal of volatile organic compounds, Catalysts 6 (2016) 7, https://doi.org/10.3390/catal6010007.
[3] S. Cheng, J. Zhang, Y. Wang, D. Zhang, G. Teng, G.-P. Chang-Chien, Q. Huang, Y.-B. Zhang, P. Yan, Global research trends in health effects of volatile organic compounds during the last 16 years: a bibliometric analysis, Aerosol Air Qual. Res. 19 (2019) 1834–1843, https://doi.org/10.4209/aaqr.2019.06.0327.
[4] J.W. Kwon, H.W. Park, W.J. Kim, M.G. Kim, S.J. Lee, Exposure to volatile organic compounds and airway inflammation, Environ. Health 17 (2018) 65, https://doi.org/10.1186/s12940-018-0410-1.
[5] F.I. Khan, A.K. Ghoshal, Removal of volatile organic compounds from polluted air, J. Loss Prev. Process Ind. 13 (2000) 527–545, https://doi.org/10.1016/S0950-4230(00)00007-3.
[6] A. Berenjian, N. Chan, H.J. Malmiri, Volatile organic compounds removal methods: a review, Am. J. Biochem. Biotechnol. 8 (2012) 220–229, https://doi.org/10.3844/ajbbsp.2012.220.229.
[7] A. Buekens, Thermal and catalytic combustion, in: B. Nath, G. Stefanov Cholakov (Eds.), Pollution Control Technologies, Encyclopedia of Life Support Systems, 2009, pp. 352–360.
[8] M.S. Kamal, S.A. Razzak, M.M. Hossain, Catalytic oxidation of volatile organic compounds (VOCs) – a review, Atmos. Environ. 140 (2016) 117–134, https://doi.org/10.1016/j.atmosenv.2016.05.031.
[9] S. Song, S. Zhang, X. Zhang, P. Verma, M. Wen, Advances in catalytic oxidation of volatile organic compounds over Pd-supported catalysts: recent trends and challenges, Front. Mater. 7 (2020), 595667, https://doi.org/10.3389/fmats.2020.595667.
[10] J.C. Védrine, Metal oxides in heterogeneous oxidation catalysis: state of the art and challenges for a more sustainable world, Chem. Sus. Chem. 12 (2018) 577–588, https://doi.org/10.1002/cssc.201802248.
[11] R.Z. Yarbay Şahin, M. Duplančić, V. Tomašić, J.H. Badia i Córcoles, S. Kurajica, Essential role of B metal species in perovskite type catalyst structure and activity on toluene oxidation, Int. J. Environ. Sci. Technol. 19 (2021) 553–564, https://doi.org/10.1007/s13762-021-03148-x.
[12] L. Liu, J. Sun, J. Ding, Y. Zhang, J. Jia, T. Sun, Catalytic oxidation of VOCs over $SmMnO_3$ perovskites: catalyst synthesis, change mechanism of active species, and degradation path of toluene, Inorg. Chem. 58 (2019) 14275–14283, https://doi.org/10.1021/acs.inorgchem.9b02518.
[13] A. Žužić, L. Pavić, A. Bafti, S. Marijan, J. Macan, A. Gajović, The role of the A-site cation and crystal structure on the electrical conductivity of strontium-doped calcium and barium manganites, J. Alloys Compd. 935 (2023), 167949, https://doi.org/10.1016/j.jallcom.2022.167949.
[14] A. Žužić, J. Macan, Permanganometric determination of oxygen nonstoichiometry in manganites, Open Ceram. 5 (2021), 100063, https://doi.org/10.1016/j.oceram.2021.100063.
[15] D.P. Kozlenko, N.T. Dang, T.L. Phan, S.E. Kichanov, L.H. Khiem, S.G. Jabarov, T. A. Tran, T.V. Manh, A.T. Le, T.K. Nguyen, B.N. Savenko, The structural, magnetic and vibrational properties of Ti-doped $BaMnO_3$, J. Alloys Compd. 695 (2017) 2539–2548, https://doi.org/10.1016/j.jallcom.2016.11.159.
[16] B. Poojitha, A. Rathore, S. Saha, Spin-phonon coupling in Sr and Ti incorporated 9R-$BaMnO_3$, J. Magn. Magn. Mater. 483 (2019) 212–218, https://doi.org/10.1016/j.jmmm.2019.03.114.
[17] S. Berbeth Mary, M. Francis, V.G. Sathe, V. Ganesan, A.L. Rajesh, Enhanced thermoelectric property of nanostructured $CaMnO_3$ by sol-gel hydrothermal method, Phys. B Condens. Matter 575 (2019), 411707, https://doi.org/10.1016/j.physb.2019.411707.
[18] S. Majumdar, H. Huhtinen, P. Paturi, R. Palai, The effect of oxygen on the Jahn-teller distortion and magnetization dynamics of $Pr_{0.9}Ca_{0.1}MnO_3$ thin films, J. Phys. Condens. Matter 25 (2012), 066005, https://doi.org/10.1088/0953-8984/25/6/066005.
[19] C.H. Shek, G.M. Lin, J.K.L. Lai, Effect of oxygen deficiency on the Raman spectra and hyperfine interactions of nanometer SnO_2, Nanostruct. Mater. 11 (1999) 831–835, https://doi.org/10.1016/S0965-9773(99)00373-6.
[20] A. Žužić, F. Car, J. Macan, V. Tomašić, A. Gajović, Simultaneous oxidation of aromatic compounds using Sr-doped lanthanum manganites as catalysts, Int. J. Appl. Ceram. Technol. 19 (2022) 2891–2904, https://doi.org/10.1111/ijac.14068.
[21] A.E. Danks, S.R. Hall, Z. Schnepp, The evolution of 'sol–gel' chemistry as a technique for materials synthesis, Mater. Horiz. 3 (2016) 91–112, https://doi.org/10.1039/C5MH00260E.
[22] P. Scherrer, Bestimmung der Größe und der inneren Struktur von Kolloidteilchen mittels Röntgenstrahlen, Nachr, Ges. Wiss. Gottingen, Math.-Phys. Kl. 1918 (1918) 98–100.
[23] P. Koralli, S.F. Varol, G. Mousdis, D.E. Mouzakis, Z. Merdan, M. Kompitsas, Comparative studies of undoped/Al-doped/in-doped ZnO transparent conducting oxide thin films in optoelectronic applications, Chemosensors 10 (2022) 162, https://doi.org/10.3390/chemosensors10050162.
[24] V. Berbenni, C. Milanese, G. Bruni, P. Cofrancesco, A. Marini, Solid state synthesis of $CaMnO_3$ from $CaCO_3$-$MnCO_3$ mixtures by mechanical energy, Z. Naturforsch. 61 (2006) 281–286, https://doi.org/10.1515/znb-2006-0307.
[25] A. Gagrani, S. Sousa, O.C. Monteiro, T. Tsuzuki, Solid state synthesis and photocatalytic activity of bio-inspired calcium manganese oxide catalysts, J. Solid State Chem. 288 (2020), 121390, https://doi.org/10.1016/j.jssc.2020.121390.
[26] N. Rezlescu, E. Rezlescu, P.D. Popa, C. Doroftei, M. Ignat, Characterization and catalytic properties of some perovskites, Compos. B Eng. 60 (2014) 515–522, https://doi.org/10.1016/j.compositesb.2014.01.006.
[27] F. Duprat, Light-off curve of catalytic reaction and kinetics, Chem. Eng. Sci. 57 (2002) 901–911, https://doi.org/10.1016/j.jcat.2003.11.01.
[28] M. Johnsson, P. Lemmens, Crystallography and chemistry of perovskites, in: H. Kronmüller, S. Parkin (Eds.), Handbook of Magnetism and Advanced Magnetic Materials, John Wiley & Sons, 2007, pp. 1–9, https://doi.org/10.1002/9780470022184.hmm411.
[29] T. Sato, S. Takagi, S. Deledda, B.C. Hauback, S. Orimo, Extending the applicability of the Goldschmidt tolerance factor to arbitrary ionic compounds, Sci. Rep. 6 (2016) 23592, https://doi.org/10.1038/srep23592.
[30] P. Mars, D.W. van Krevelen, Oxidations carried out by means of vanadium oxide catalysts, Chem. Eng. Sci. 3 (1954) 41–59, https://doi.org/10.1016/S0009-2509(54)80005-4.
[31] D. Alami, Environmental applications of rare-earth manganites as catalysts: a comparative study, Environ. Eng. Res. 18 (2013) 211–219, https://doi.org/10.4491/eer.2013.18.4.211.
[32] R.B. Dudek, X. Tian, M. Blivin, L.M. Neal, H. Zhao, F. Li, Perovskite oxides for redox cracking of *n*-hexane under a cyclic redox scheme, Appl. Catal. B 246 (2019) 30–40, https://doi.org/10.1016/j.apcatb.2019.01.048.
[33] F. Hao, Y. Gao, L. Neal, R.B. Dudek, W. Li, C. Chung, B. Guan, P. Liu, X. Liu, F. Li, Sodium tungstate-promoted $CaMnO_3$ as an effective, phase-transition redox catalyst for redox oxidative cracking of cyclohexane, J. Catal. 385 (2020) 213–223, https://doi.org/10.1016/j.jcat.2020.03.022.
[34] N. Dewi, W. Setyarini, R. Anggraini, S.S. Siregar, A. Awaluddin, The novel synthesis of $CaMnO_3$ perovskite type-oxide and its catalytic activity for degradation of dye, J. Phys. Conf. Ser. 1655 (2020), 012040, https://doi.org/10.1088/1742-6596/1655/1/012040.
[35] T. Wang, X. Qian, D. Yue, X. Yan, H. Yamashita, Y. Zhao, $CaMnO_3$ perovskite nanocrystals for efficient peroxydisulfate activation, Chem. Eng. J. 398 (2020), 125638, https://doi.org/10.1016/j.cej.2020.125638.
[36] A. Mishra, N. Galinsky, F. He, E.E. Santiso, F. Li, Perovskite-structured $AMn_xB_{1-x}O_3$ (a = ca or Ba; B = Fe or Ni) redox catalysts for partial oxidation of methane, Catal, Sci. Technol. 6 (2016) 4535–4544, https://doi.org/10.1039/c5cy02186c.
[37] H. Ning, W. Ji, Y. Li, C. Zhang, Engineering the mechanically mixed $BaMnO_3$-CeO_2 catalyst for NO direct decomposition: effect of thermal treatment on catalytic activity, Catalysts 13 (2023) 259, https://doi.org/10.3390/catal13020259.
[38] T. Ye, Z. Chen, Y. Chen, Q. Zhong, H. Qu, Mesoporous–optimized $BaMnO_3$ perovskite small-scale nanocrystals in SSZ-13 to enhance activity for the selective catalytic reduction reaction of NO, Appl. Catal. A Gen. 647 (2022), 118890, https://doi.org/10.1016/j.apcata.2022.118890.
[39] S. Gholamrezaei, M. Ghanbari, O. Amiri, M. Salavati-Niasari, L.K. Foong, $BaMnO_3$ nanostructures: simple ultrasonic fabrication and novel catalytic agent toward oxygen evolution of water splitting reaction, Ultrason. Sonochem. 61 (2020), 104829, https://doi.org/10.1016/j.ultsonch.2019.104829.
[40] F.V.E. Hensling, C. Xu, F. Gunkel, R. Dittmann, Unraveling the enhanced oxygen vacancy formation in complex oxides during annealing and growth, Sci. Rep. 7 (2017) 39953, https://doi.org/10.1038/srep39953.
[41] P.S. Liu, G.F. Chen, Porous Materials, Processing and Applications, Butterworth-Heinemann, 2014, pp. 21–112.